

# R<sup>2</sup>Det: Redemption from Range-view Representation for Accurate 3D Object Detection

Yihan Wang<sup>1</sup>, Qiao Yan<sup>1</sup>, Yi Wang<sup>2</sup>

<sup>1</sup>Nanyang Technological University

<sup>2</sup>The Hong Kong Polytechnic University

WANG1517@e.ntu.edu.sg, QIAO003@e.ntu.edu.sg, yi-eie.wang@polyu.edu.hk

## Abstract

LiDAR-based 3D object detection is of paramount importance for autonomous driving. Recent trends show a remarkable improvement for bird’s-eye-view (BEV) based and point-based methods as they demonstrate superior performance compared to range-view counterparts. This paper presents an insight that leverages range-view representation to enhance 3D points for accurate 3D object detection. Specifically, we introduce a Redemption from Range-view Module (R<sup>2</sup>M), a plug-and-play approach for 3D surface texture enhancement from the 2D range view to the 3D point view. R<sup>2</sup>M comprises BasicBlock for 2D feature extraction, Hierarchical-dilated (HD) Meta Kernel for expanding the 3D receptive field, and Feature Points Redemption (FPR) for recovering 3D surface texture information. R<sup>2</sup>M can be seamlessly integrated into state-of-the-art LiDAR-based 3D object detectors as preprocessing and achieve appealing improvement, e.g., 1.39%, 1.67%, and 1.97% mAP improvement on easy, moderate, and hard difficulty level of KITTI *val* set, respectively. Based on R<sup>2</sup>M, we further propose R<sup>2</sup>Detector (R<sup>2</sup>Det) with the Synchronous-Grid RoI Pooling for accurate box refinement. R<sup>2</sup>Det outperforms existing range-view-based methods by a significant margin on both the KITTI benchmark and the Waymo Open Dataset. Codes will be made publicly available.

## Introduction

The LiDAR sensor plays a fundamental role in enabling the perception system for autonomous driving. However, the current scene understanding methods heavily rely on expensive 3D point cloud data generated by LiDAR sensors. To address this cost challenge, emerging LiDAR sensors that output range images have rapidly gained notice in recent years (Sun et al. 2021). These sensors offer a significant cost advantage, nearly four times cheaper than LiDAR systems generating point clouds. Additionally, range image-based LiDAR sensors establish a perfect 1-to-1 relationship between a pixel and a 3D point without discrete or resampling steps involved (Nowak, Ćwian, and Skrzypczyński 2021). Due to this clear relationship between pixels and 3D points, those LiDAR sensors hold great potential for providing precise 3D semantic information. Motivated by this potential, several related works on semantic scene segmentation have been developed, such as (Milioto et al. 2019; Wu et al. 2018; Chen and Chang 2022; Hu et al. 2020; Cheng, Han, and Xiao 2023).

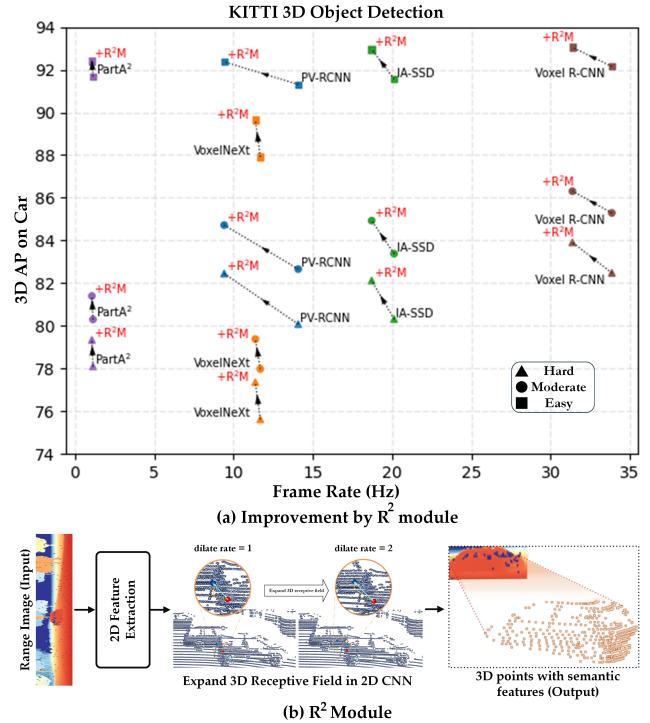


Figure 1: (a) Our proposed plug-and-play R<sup>2</sup> Module improves the performance of existing 3D object detectors at a small cost of inference speed. (b) The sketch of R<sup>2</sup> Module. It encodes the input range images with 2D features by expanding the 3D receptive field and outputs 3D points with semantic features.

However, the potential of pixel-wise semantics has yet to be fully harnessed in the task of 3D object detection. Despite the attempts by existing 3D point-wise methods (Qi et al. 2017b,c; Zhang et al. 2022; Zheng et al. 2023; Chen et al. 2022) to alleviate computational burdens through set abstraction or downsampling modules, these methods still face challenges in terms of efficiency for practical implementation. On the other hand, there is another kind of methods that rely on BEV (or voxels) (Mao et al. 2021b; Zhou et al. 2023; He et al. 2022; Chen et al. 2023), offering faster inference times, but they still struggle to achieve satisfactory

levels of accuracy. Point-view and BEV methods have received thorough investigation, but range-view methods remain relatively underexplored. The information provided by range-view representation has not been fully leveraged in existing approaches.

As previously highlighted, range images establish a direct correspondence between pixels and their corresponding 3D points. This implies a more effective acquisition of semantic information for each 3D point from range images, i.e., extracting features within the 2D plane and subsequently translating them back to 3D points. This is an advantage over conventional 3D point-wise feature extraction techniques in terms of computational complexity. However, existing range-view-based 3D detectors (Liang et al. 2021; Fan et al. 2021; Meyer et al. 2019; Bewley et al. 2020) process range images directly based on 2D CNN backbones. While efficient, they overlook a crucial issue, the loss of 3D surface texture information prevalent in 2D range images. This particular information encapsulates the interrelations among points within the point clouds. For instance, as depicted in Fig. 1(b), while range images uphold the relative spatial distances between points, they unavoidably omit *all* the 3D surface information, which fundamentally contributes to the intricate relationships among points in 3D coordinates.

In this paper, we address the abovementioned challenges through a meticulously designed Redemption from Range-view Module ( $R^2M$ ), a plug-and-play manner to extract 3D surface textures from 2D range images, as shown in Fig. 1(b). First,  $R^2M$  comprises a BasicBlock and a novel Hierarchical-dilated (HD) Meta Kernel. This combination effectively enhances 2D range-view point-wise semantic features by addressing variations in object sizes and significantly expanding the 3D receptive field. Second, to counter the loss of 3D surface texture information inherent in range images, we introduce the Feature Points Redemption (FPR). The FPR retrieves the lost information and transforms semantic feature points into 3D space, thereby reinstating object surface textures and minimizing the impact of the 3D information loss inherent in 2D range-view representation. Importantly, this feature extraction operation is considerably more efficient than existing 3D point-wise extraction methods. The 3D points generated by the  $R^2M$  inherently contain semantic information. As a result, these points can be seamlessly integrated into the input stage of existing single-modality-based 3D object detectors, enhancing their input data and subsequently improving performance on all three difficulty levels of KITTI *val* set, as shown in Fig. 1(a). Moreover, we build the  $R^2$ Detector ( $R^2Det$ ) with the proposed Synchronous-Grid (S-Grid) RoI Pooling strategy for box refinement, which uses two different grid sizes in parallel to aggregate region-of-interest (RoI) features from each proposal. This multi-sampling approach facilitates the abstraction of more contextual features, leading to more accurate box prediction.

Our contributions can be summarized as follows. (1) We propose an efficient plug-and-play  $R^2M$ , which enhances the 2D feature extraction by expanding the 3D receptive field and provides an elegant strategy for resolving the 3D surface texture loss and exploring the point-wise semantics of range images. (2) We introduce  $R^2Det$ , a novel approach that

addresses the limitations of range-view representation and enables more accurate 3D object detection. (3) We perform exhaustive trials on both the KITTI dataset (Geiger, Lenz, and Urtasun 2012) and the Waymo Open Dataset (Sun et al. 2020). As a result, our proposed  $R^2$  module can boost 3D object detectors consistently with small frame rate sacrifice (see Table 1). Our proposed  $R^2Det$  outperforms existing range-view-based methods significantly and achieves state-of-the-art performance on both datasets.

Method	AP <sub>3D</sub> (%)		
	Easy	Mod.	Hard
PV-RCNN (Shi et al. 2020)	91.31	82.66	80.08
$R^2M$ +PV-RCNN	92.37	84.72	82.45
<i>Improvement</i>	<i>+1.06</i>	<i>+2.06</i>	<i>+2.37</i>
VoxelNeXt(Chen et al. 2023)	87.92	77.98	75.62
$R^2M$ +VoxelNeXt	89.65	79.38	77.36
<i>Improvement</i>	<i>+1.73</i>	<i>+1.40</i>	<i>+1.73</i>
IA-SSD(Zhang et al. 2022)	91.57	83.38	80.32
$R^2M$ +IA-SSD	92.96	84.93	82.12
<i>Improvement</i>	<i>+1.39</i>	<i>+1.55</i>	<i>+1.80</i>

Table 1: Effect of the  $R^2$  Module on the KITTI *val* split with AP calculated by 40 recall positions.

## Related Work

**3D Object Detection on Point Clouds.** Point clouds remain a favored input representation due to their accurate depth information and resilience to various weather conditions. However, the substantial volume of unstructured data poses an initial challenge in determining the appropriate input data representation. Some efforts have been made to project point clouds into multiple views (Ku et al. 2018; Chen et al. 2017; Zhou et al. 2020; Liang et al. 2018; Yang, Liang, and Urtasun 2018), relying on manual feature extraction. Continuous works (Zhou and Tuzel 2017; Lang et al. 2019; Deng et al. 2021a; He et al. 2022; Mao et al. 2021b; Zhou et al. 2023; Yang et al. 2023a) have replaced the manual step with a learnable end-to-end voxel feature abstraction module. These voxelization-based methods offer higher efficiency but often suffer from unsatisfactory accuracies.

Contrasting with approaches relying on the hybrid view and voxels, PV-based methods establish object identification relative to individual points. Initial works like (Qi et al. 2017a; Wang and Jia 2019; Yang et al. 2018) integrate (Qi et al. 2017b,c) into their frameworks. PointRCNN (Shi, Wang, and Li 2019) introduces a revolutionary box refinement module. Despite considerable accuracy improvements, these methods still grapple with latency concerns. 3DSSD (Yang et al. 2020) employs a set abstraction layer to downsample point clouds and mitigate latency. Similarly, SASA (Chen et al. 2022) advances latency reduction by introducing an innovative set abstraction module for foreground point segmentation. DTSSD (Zheng et al. 2023) proposes a central density-aware enhancement module to address latency. Further latency reduction remains an ongoing challenge.

**3D Object Detection on Range Images.** The solution for transplanting the fully convolutional network onto the RV of point clouds is investigated by (Li, Zhang, and Xia

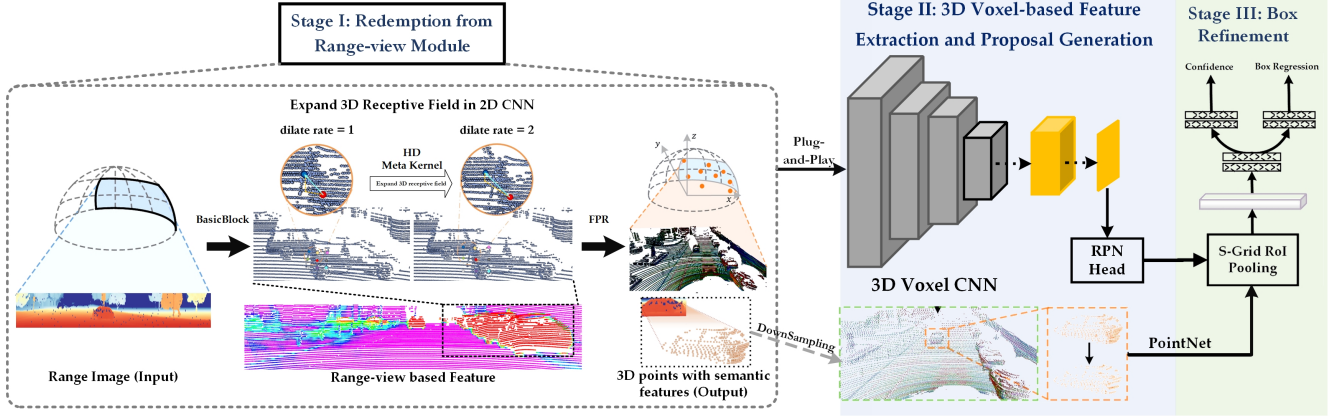


Figure 2: Architecture of our proposed R<sup>2</sup>Det. The range images are initially processed through a BasicBlock and the HD Meta Kernel. The FPR module transforms these images from 2D semantic pixels to 3D points with surface texture features. Then 3D feature points are voxelized and fed into a 3D sparse convolution-based backbone. This backbone encodes multi-scale semantic features and generates 3D proposals. Meanwhile, the redeemed feature points from range images are downsampled. Finally, these downsampled features and candidate boxes are passed through the S-Grid RoI Pooling to refine the candidate boxes.

2016). Based on this approach, LaserNet (Meyer et al. 2019) predicts the probability of bounding boxes for representing the uncertainty of detection using 2D CNNs. (Bewley et al. 2020) similarly uses 2D CNNs while it novelly presents a dynamic adjustable dilate rate mechanism for adapting the scale variation caused by range images. In comparison to (Bewley et al. 2020), (Liang et al. 2020) and its continuous work (Liang et al. 2021) extract RV feature maps with multiple dilate rates. (Sun et al. 2021) proposes to regress 3D boxes by transferring foreground points from the RV to the PV. Innovatively, RangeDet (Fan et al. 2021) exploits point cloud geometric information from RV for feature extraction.

## Methodology

### Overall Architecture

Figure 2 presents the schematic for the entire structure of R<sup>2</sup>Det. The input to the system is a five-channel range view of a point cloud (also known as a range image), which includes x, y, z, intensity, and range data. The range image is firstly encoded by a BasicBlock (He et al. 2015), then the output feature maps are stacked into Hierarchical-dilated (HD) Meta Kernel. The output 2D feature map is transferred from the range view to the point view in the Feature Points Redemption (FPR) module. These steps form Stage I: R<sup>2</sup>M. Afterward, these 3D feature points are split into two streams. One is partitioned into voxels and fed into 3D voxel CNNs for proposal generation, and the other is downsampled into a set of keypoints. Finally, the generated candidate boxes and the downsampled keypoints are fed into the Synchronous-Grid (S-Grid) RoI pooling module for box refinement.

### Stage I: Redemption from Range-view Module

**Range-view Feature Extraction.** Benefiting from incorporating 3D geometric information into 2D CNN, *Meta-kernel* convolutional layer proposed in (Fan et al. 2021) outperformed conventional 2D CNNs. Inspired by this, we introduce a straightforward yet impactful module, Hierarchical Di-

lated (HD) Meta-kernel. This module enhances the utilization of 3D geometric information within 2D CNNs, leading to improved performance. Additionally, our approach innovatively extends the 3D receptive field in 2D CNNs. This extension allows for the dynamic generation of adapted weights from related 3D coordinates, addressing scale variation challenges in range images.

Similar to *Meta-kernel* (Fan et al. 2021), the HD Meta Kernel can also be decomposed into the feature sampler, the element-wise processor, and the feature accumulator. Different from *Meta-kernel*, we incorporate another dilate rate branch in the feature sampler, and the feature accumulator also differs. As a result, the feature sampler can be formalized as two kernels  $\mathcal{K}_1$  and  $\mathcal{K}_2$ :

$$\mathcal{K}_1 = \{(d_h^1, d_w^1) | d_h^1, d_w^1 \in [-1, 1], d_h^1, d_w^1 \in \mathbb{Z}\} \quad (1)$$

$$\mathcal{K}_2 = \{(d_h^2, d_w^2) | d_h^2 = 2d_h^1, d_w^2 = 2d_w^1\} \quad (2)$$

And the feature accumulator can be described as follows:

$$O_{l_o} = \text{Concat}(\text{FC}(\text{Concat}(I_{l_o \leftrightarrow l_n})), \text{FC}(\text{Concat}(I_{l_o' \leftrightarrow l_n'}))) \quad (3)$$

where  $o, o'$  define the sampling site in each stream and  $n, n' = \{0, 1, \dots, 7, 8\}$  are the corresponding nearest eight neighbors,  $I_{l_o \leftrightarrow l_n}$  denotes the output features from the element-wise processor, **FC** and **Concat** represent the fully connected layer and the concatenating process respectively.

**Feature Points Redemption.** In the FPR step, range-view feature points are transformed into point-view representation and subsequently processed by 3D CNNs. The one-to-one mapping  $\Pi : \mathbb{R}^2 \mapsto \mathbb{R}^3$  between each pixel  $(u, v)$  at the range image and each point  $p = (x, y, z)$  is established as Eq.(4):

$$\begin{aligned} x &= \sqrt{\frac{r^2 \{1 - \sin^2((1 - v/h)\mathbf{F} - \mathbf{F}_{up})\}}{\sec^2\{(1 - 2u/w)/\pi\}}} \\ y &= x \cdot \tan\{(1 - 2u/w)/\pi\} \\ z &= \sin\{(1 - v/h)\mathbf{F} - \mathbf{F}_{up}\}r \end{aligned} \quad (4)$$

where  $\mathbf{F} = \mathbf{F}_{up} + \mathbf{F}_{down}$  is the vertical field-of-view,  $(h, w)$  are the height and width of the projected range image,  $r$  is the range value of each pixel. Thus, each pixel  $I_{(u,v)} = f^{(64)}$  carrying with a feature embedding of surface texture information are projected back into the corresponding point  $\mathbf{p} = [x, y, z, i, f^{(64)}]$  via this mapping ( $\Pi : \mathbb{R}^2 \mapsto \mathbb{R}^3$ ), where  $i$  denotes its intensity.

Through the FPR module, the 2D semantic feature points extracted from the range view are seamlessly integrated with the 3D point clouds, effectively enabling the exploitation of the semantic information for further 3D object detection. Essentially, this module harmonizes the 2D semantic feature points derived from the range view with the 3D point cloud. These points are subsequently re-transformed into their 3D coordinates and further encoded by 3D CNNs. Since the 3D CNNs can extract 3D surface texture information, they mitigate the inherent limitations of the range-view representation. Overall, this plug-and-play module demonstrates remarkable efficiency and efficacy compared to point-wise processing methods like IA-SSD(Zhang et al. 2022) for the 3D object detection task, as validated through Table 1.

**R<sup>2</sup> Module.** Our proposed R<sup>2</sup>M combines the Range-view Feature Extraction and FPR components to create a unified structure. This structure enhances the utilization of range-view feature representation for 3D object detection. On the one hand, leveraging the dense semantic information in range images compared to 3D sparse points, the R<sup>2</sup>M exploits these dense 2D features and integrates geometric information by expanding the receptive field in 3D space through HD Meta Kernel. This expansion significantly contributes to enhancing detection accuracy. On the other hand, the FPR module smoothly converts all redeemed feature points into 3D space, enabling efficient processing and seamless integration of the R<sup>2</sup>M into existing LiDAR-based 3D object detectors. As illustrated in Table 1, the R<sup>2</sup>M enhances the input-level 3D points with range-view semantic features, leading to improved detection performance across various 3D detectors.

## Stage II: 3D Voxel-based Feature Extraction and Proposal Generation

Previous 3D detectors (Shi et al. 2020; Deng et al. 2021a; Yan, Mao, and Li 2018; Graham and van der Maaten 2017; Zhou and Tuzel 2017) frequently utilize voxel-based 3D sparse convolution to transform point clouds into sparse 3D volumes and embeds them with extracted voxel-wise features. The resulting tensors are subsequently layered along the Z axis to generate feature maps in the bird’s-eye view. For its efficacy and precision, we employ it as the 3D backbone of our framework for 3D texture feature capture and 3D proposal generation from the redeemed feature points. More detailed descriptions on Stage II are provided in sup. material.

With the seamless connection of range-view and voxel-wise processing, R<sup>2</sup>Det extracts versatile features from flexible viewpoints, offering both complementary 2D semantic and 3D texture information. In contrast to range-view-based methods (Fan et al. 2021; Liang et al. 2021; Sun et al. 2021; Meyer et al. 2019; Bewley et al. 2020; Liang et al. 2020), which excel in 2D semantic features but lack 3D surface

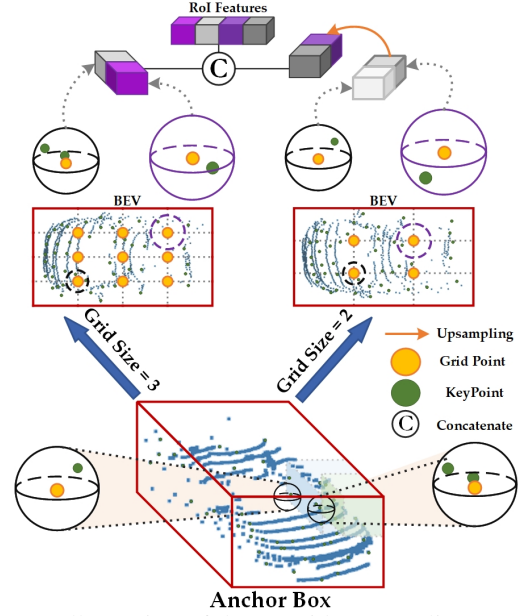


Figure 3: Illustration of the S-Grid RoI Pooling module. A slight change in the sampling site (Grid Point) causes considerably different feature distribution of sampled keypoints.

texture information due to limitations of range images, our R<sup>2</sup>Det addresses and mitigates this issue by employing subsequent 3D CNNs to restore 3D texture information from the redeemed feature points in the range view. Unlike multi-view approaches (Zhou et al. 2020; Chen et al. 2017; Wang et al. 2020; Deng et al. 2021b), which typically require fusing 2D views of point clouds, the FPR strategy facilitates feature extraction across multiple dimensions directly from the 3D point cloud naturally generated from the range image, eliminating the need for fusion stages.

## Stage III: Box Refinement

Since redeemed feature points are separated into regular voxels globally in the prior modules, and candidate anchors are positioned in the bird’s-eye view, this section identifies local features to facilitate the refinement of candidate boxes. This section is comprised of three subsections: the global scenario representation, the local RoI feature extraction, and the box refinement. **Global Scenario Representation.** As the 3D voxel CNNs serve as the 3D backbone of our model, a straightforward option for this step is directly implementing the Voxel Set Abstraction (VSA) paradigm proposed in (Shi et al. 2020). In the VSA, the PointNet block(Qi et al. 2017b) transforms each level of voxel-wise features and concatenates them together. However, this procedure involves processing and storing large amounts of data, resulting in demanding computational requirements and longer training time.

Given the limitations of VSA, we opt to apply the Furthest Point Sampling (Qi et al. 2017c) algorithm to downsample  $\mathcal{P}$  into a set of representative points  $\mathcal{R} = \{\mathbf{p}_j | \forall \mathbf{p}_j \in \mathcal{P}, j = [0, C - 1]\}$ , where  $C$  specifies the size of the point set. Subsequently, the redeemed feature points undergo another round of feature extraction using the PointNet block within the PV.

Method	Input View	Car AP <sub>3D</sub> (%)			Car AP <sub>BEV</sub> (%)		
		Easy	Moderate	Hard	Easy	Moderate	Hard
CAT-Det(Zhang, Chen, and Huang 2022)	MV	89.87	81.32	76.68	92.59	90.07	85.82
EPNet++(Liu et al. 2022)	MV	<b>91.37</b>	81.96	76.71	<b>95.41</b>	89.00	85.73
MVMM(Li et al. 2023)	MV	87.59	78.87	73.78	92.17	88.70	85.47
PVT-SSD(Yang et al. 2023b)	MV	90.65	82.29	76.85	95.23	<b>91.63</b>	<b>86.43</b>
DVF-PV(Mahmoud, Hu, and Waslander 2023)	MV	90.99	<b>82.40</b>	<b>77.37</b>	-	-	-
Voxel R-CNN (Deng et al. 2021a)	BEV	<b>90.90</b>	81.62	77.06	<b>94.85</b>	88.83	86.13
VoxSeT(He et al. 2022)	BEV	88.53	82.06	77.46	92.70	89.07	86.29
BSAODet(PV-RCNN++)(Xiao et al. 2023)	BEV	88.66	81.95	77.40	92.66	88.90	86.23
OcTr(Zhou et al. 2023)	BEV	90.88	<b>82.64</b>	<b>77.77</b>	93.08	<b>89.56</b>	<b>86.74</b>
GD-MAE(Yang et al. 2023a)	BEV	88.14	79.03	73.55	94.22	88.82	83.54
PointRCNN(Shi, Wang, and Li 2019)	PV	86.96	75.64	70.70	92.13	87.39	82.72
3DSSD(Yang et al. 2020)	PV	88.36	79.57	74.55	92.66	89.02	85.86
IA-SSD(multi) (Zhang et al. 2022)	PV	88.34	80.13	75.04	92.79	89.33	84.35
SASA (Chen et al. 2022)	PV	<b>88.76</b>	<b>82.16</b>	<b>77.16</b>	<b>92.87</b>	<b>89.51</b>	<b>86.35</b>
DTSSD(Zheng et al. 2023)	PV	88.62	79.94	74.91	92.77	89.18	86.03
RangeRCNN (Liang et al. 2020)	RV	88.47	81.33	77.09	92.15	88.40	85.74
RCD(Bewley et al. 2020)	RV	70.54	60.56	55.58	82.26	75.83	69.61
RangeIoUDet(Liang et al. 2021)	RV	88.60	79.80	76.76	92.28	88.59	85.83
RangeDet (Fan et al. 2021)	RV	85.41	77.36	72.60	90.93	87.67	82.92
R <sup>2</sup> Det (ours)	RV	<b>90.93</b>	<b>82.42</b>	<b>77.84</b>	<b>93.02</b>	<b>91.17</b>	<b>86.62</b>

Table 2: Comparison on the KITTI online *test* server. AP with an IoU threshold of 0.7 for *Cars* and 40 recall positions are conducted to evaluate the results. 80% of the total *train+val* data is used for training. MV, BEV, PV and RV refer to methods with input from multiple views, bird’s-eye view, point view and range view.

These simple operations aim to enrich contextual data, facilitating subsequent proposals refinement module. Compared with the VSA module, we provide a direct yet more appropriate solution for processing the redeemed feature points.

**Local RoI Feature Extraction.** The RoI-grid pooling algorithm in PV R-CNN inspires us to aggregate RoI features from each grid point using surrounding keypoints. However, the keypoints within a certain radius have a sensitive structure that highly depends on their sampling position. Even a small adjustment to the sampling site can lead to very different feature aggregation, as shown in Figure 3.

As shown in Figure 3, feature distribution is susceptible to (1) sampling radii and (2) grid sizes. Consequently, we partition the candidate box into two grid sizes of 3 and 2, and then apply RoI-grid pooling with distinct sampling radii in each branch. The resulting refined features are then concatenated to form RoI features. Particularly, an upsampling module is implemented in the rough partition (Grid Size = 2) branch to achieve uniform scaling prior to concatenation. Compared with the RoI-grid Pooling strategy, the proposed S-Grid RoI Pooling leverages more comprehensive contextual information for each proposal.

**Detect Head.** After RoI pooling, the detect head predicts a confidence score related to Intersection over Union (IoU) and conducts additional regression on the box coordinates for each region proposal. The refinement network consists of a two-layer Multilayer Perceptron (MLP) according to (Shi et al. 2020) with separate branches for confidence prediction and box refinement.

## Training Loss

The training process of R<sup>2</sup>Det is end-to-end optimized, whose total training loss can be calculated as:

$$\mathcal{L}_T = \mathcal{L}_{rpn} + \mathcal{L}_{rea} + \mathcal{L}_{ref} \quad (5)$$

where  $\mathcal{L}_{rpn}$  represents the loss of the proposal generation module referring to (Yan, Mao, and Li 2018),  $\mathcal{L}_{rea}$  and  $\mathcal{L}_{ref}$  denote the training objective of the weight reassignment module and the training loss of the box refinement module according to (Shi et al. 2020). For more detailed information on training losses, please refer to the sup. file.

## Experiments

We conduct experiments on both the KITTI dataset and the Waymo Open Dataset. For the KITTI dataset, we follow the official *train/val* split. More detailed configuration of the pipeline is provided in the sup. file.

### Detection Results on KITTI Dataset

As shown in Table 2, R<sup>2</sup>Det achieves the state-of-the-art (SOTA) performance on the KITTI *test* set thanks to R<sup>2</sup>M utilizing the range-view representation to its full potential. It outperforms all range-view-based methods at all difficulty levels. Generally, R<sup>2</sup>Det achieves 77.84% on the hard level of *Car* in AP<sub>3D</sub>, beating other MV, BEV, and PV-based algorithms.

For a comprehensive comparison, we also provide the performance of the KITTI *val* split with mAP derived from 11 recall positions. According to Table 3, our R<sup>2</sup>Det has the strongest effect on the *val* split at the moderate and hard

Method	Car AP <sub>3D</sub> (%)		
	Easy	Mod.	Hard
<b>Multiple View Input:</b>			
H <sup>2</sup> 3D R-CNN(Deng et al. 2021b)	89.63	85.20	79.08
CAT-Det(Zhang, Chen, and Huang 2022)	90.12	81.46	79.15
EPNet++(Liu et al. 2022)	<b>92.51</b>	<b>83.17</b>	<b>82.27</b>
<b>Single View Input:</b>			
PointPillars(Lang et al. 2019)	86.62	76.06	68.91
PV-RCNN(Shi et al. 2020)	89.35	83.69	78.70
CIA-SSD(Zheng et al. 2020)	<b>90.04</b>	79.81	78.80
VoTr-TSD(Mao et al. 2021b)	89.04	84.04	78.68
Voxel R-CNN(Deng et al. 2021a)	89.41	84.52	78.93
IA-SSD(Zhang et al. 2022)	-	79.57	-
VoxSeT(He et al. 2022)	88.45	78.48	77.07
DTSSD(Zheng et al. 2023)	-	79.39	-
OcTr(Zhou et al. 2023)	88.43	78.57	77.16
R <sup>2</sup> Det (ours)	89.75	<b>85.78</b>	<b>79.08</b>

Table 3: Comparison on the KITTI *val* split with AP derived from 11 recall positions for *Car* class.

difficulty levels. In summary, our proposed R<sup>2</sup>Det is competitive to MV, BEV, and PV-based methods and achieves SOTA performance on range-view-based 3D object detection, as demonstrated by the results on both the *test* set and *val* split of the KITTI.

### Detection Results on Waymo Open Dataset

As the Waymo Open Dataset (WOD) is the unique dataset providing range images, we further examine the performance of R<sup>2</sup>Det on this challenging large-scale dataset.

Among the methods listed in Table 4, R<sup>2</sup>Det achieves the best results in two difficulty levels, with the highest mAP/mAPH for the *Vehicle* class and the second best mAPH for the *Pedestrian* class on Level 1 difficulty level. We can observe that R<sup>2</sup>Det is highly competitive with state-of-the-art methods on the Waymo Open Dataset, achieving the best performance on both difficulty levels for the *Vehicle* class with an mAP of 78.4% and 70.2%, respectively.

Table 5 validates the importance of addressing the issue of 3D surface texture loss, which is ignored by all existing range-view-based approaches. By recovering the 3D surface shape of objects through our R<sup>2</sup>M, R<sup>2</sup>Det outperforms existing range-view-based methods by a substantial margin of +5.53% overall. Especially, R<sup>2</sup>Det achieves absolute improvements of +7.82% in the 30 – 50m distance range and +7.79% in distances exceeding 50m.

In conclusion, our results demonstrate the superiority of R<sup>2</sup>Det for range-view-based 3D object detection on the WOD and validate our perspective outlined in Section 1.

### Ablation Study

We conduct extensive ablation experiments to assess separate portions of our proposed scheme. All models are trained on the KITTI *train* split and evaluated on the KITTI *val* split. All AP scores are calculated by 40 recall positions.

**The effectiveness of R<sup>2</sup> Module.** Table 1 indicates the substantial enhancements that our plug-and-play R<sup>2</sup>M bring to the existing 3D object detection methods. Across various

<sup>1</sup>The RSN model for the Vehicle label is RSN Car\_1f, for the Pedestrian label is RSN Ped.1f

Method	Veh. (%)		Ped.(%)	
	mAP/mAPH	mAP/mAPH	mAP/mAPH	mAP/mAPH
<b>Level 1:</b>				
†PointPillars(Lang et al. 2019)	56.6/-		59.3/-	
*PV-RCNN (Shi et al. 2020)	74.1/73.4		62.7/52.7	
RSN <i>label</i> <sup>1</sup> S_1f (Sun et al. 2021)	70.5/70.0		74.8/69.6	
RSN <i>label</i> <sup>1</sup> L_1f (Sun et al. 2021)	75.1/74.6		77.8/72.7	
IA-SSD (Zhang et al. 2022)	70.5/69.7		69.4/58.5	
VoxSeT(He et al. 2022)	74.5/74.0		72.5/65.4	
GD-MAE(Yang et al. 2023a)	77.3/76.8		80.3/72.4	
VoxelNeXt(Chen et al. 2023)	78.2/77.7		<b>81.5/76.3</b>	
BSAODet(Xiao et al. 2023)	78.3/77.6		75.9/64.4	
R <sup>2</sup> Det <sub>0.25</sub> (ours)	75.4/74.8		73.4/63.7	
R <sup>2</sup> Det(ours)	<b>78.4/77.9</b>		77.9/75.0	
<b>Level 2:</b>				
*PV-RCNN(Shi et al. 2020)	65.0/64.3		53.8/45.1	
RSN <i>label</i> <sup>1</sup> S_1f (Sun et al. 2021)	63.0/62.6		65.4/60.7	
IA-SSD (Zhang et al. 2022)	61.6/ 60.8		60.3/50.7	
VoxSeT(He et al. 2022)	66.0/65.6		-/-	
GD-MAE(Yang et al. 2023a)	68.7/68.3		<b>72.8/65.5</b>	
VoxelNeXt(Chen et al. 2023)	69.7/69.2		72.2/ <b>65.9</b>	
BSAODet(Xiao et al. 2023)	69.5/68.9		66.8/56.4	
R <sup>2</sup> Det <sub>0.25</sub> (ours)	67.3/66.7		64.3/55.6	
R <sup>2</sup> Det(ours)	<b>70.2/69.5</b>		67.0/63.2	

Table 4: Comparison on the Waymo Open Dataset with 202 validation sequences for the 3D vehicle (IoU = 0.7), pedestrian (IoU = 0.5). Subscript 0.25: using 25% training data. †: re-implemented by (Zhou et al. 2020). \*: provided by (Zhang et al. 2022)

Method	Overall	mAP <sub>3D</sub> (%)		
		<30m	30-50m	≥50m
LaserNet(Meyer et al. 2019)	52.11	70.94	52.91	29.62
RCD(Bewley et al. 2020)	66.39	86.59	65.64	40.00
RSN CarS_1f(Sun et al. 2021)	70.50	90.80	67.80	45.40
RangeDet(Fan et al. 2021)	72.85	87.96	69.03	48.88
R <sup>2</sup> Det <sub>0.25</sub> (ours)	75.36	92.00	73.17	52.15
R <sup>2</sup> Det(ours)	<b>78.38</b>	<b>92.67</b>	<b>76.85</b>	<b>56.67</b>
<b>Improvement</b>	<b>+5.53</b>	<b>+1.87</b>	<b>+7.82</b>	<b>+7.79</b>

Table 5: Comparison with other methods taking range view as input on the Waymo Open Dataset with 202 validation sequences.

categories, including point-voxel-based, voxel-based, and point-based approaches, our R<sup>2</sup>M consistently demonstrates significant improvements of 1.39%, 1.67% and 1.97% mAP improvement on easy, moderate and hard difficulty level, respectively.

**The effectiveness of HD Meta Kernel.** Table 6 shows the impact of different range-view feature extraction strategies, which contain 2 layers. The 1st layer is a residual block (RB) of BasicBlock (He et al. 2015), while the 2nd layer can be one of the RB, Meta Kernel, or HD Meta Kernel. The baseline model, which uses only one layer of BasicBlock for feature encoding, is presented in the first row. The substantial enhancement of +3.73% between the second and last rows highlights the impact of this module. Similarly, the +2.52% increment between the last two rows indicates the performance boost achieved by expanding the 3D receptive field through the HD Meta Kernel.

**The effectiveness of HD-MK and FPR in maintaining**

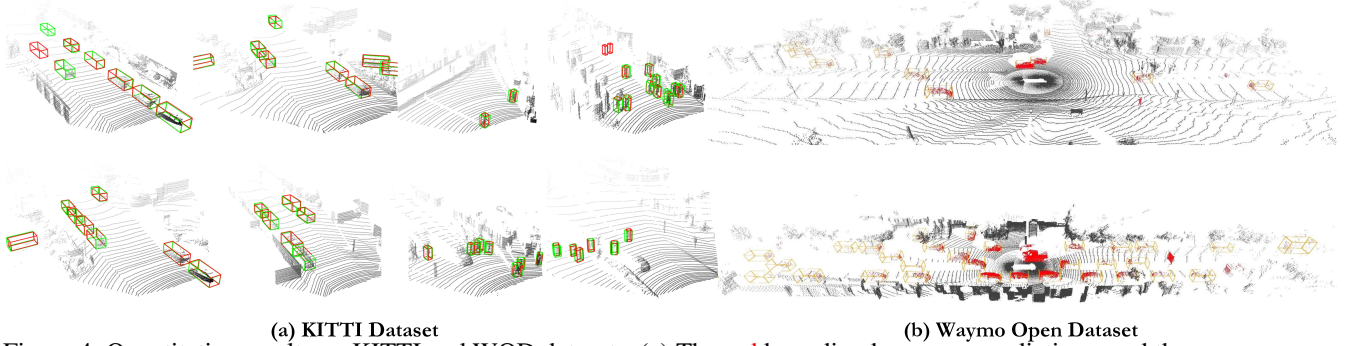


Figure 4: Quantitative results on KITTI and WOD datasets. (a) The red bounding boxes are predictions, and the green ones are ground truths. (b) The red points are ground truths, and the orange boxes are the predictions. More results refer to the sup. file.

Model	Range-view Feature Extraction				AP <sub>3D</sub> (%)
	Layer 1		Layer 2		
	RB	RB	MK	HD-MK	
Baseline	✓				81.33
R <sup>2</sup> Det	✓	✓			81.98
R <sup>2</sup> Det	✓		✓		83.19
R <sup>2</sup> Det	✓			✓	<b>85.71</b>

Table 6: Effect of the HD Meta Kernel encoding strategy on the KITTI *val* split. RB indicates the residual block (He et al. 2015), MK indicates the *Meta-kernel* convolution layer.

Range-view RB	Feature Extraction		2D to 3D		AP <sub>3D</sub> (%)
	HD-MK	U-Net+Seg.	Fore.	FPR	
✓				✓	81.33
		✓		✓	82.78
✓		✓	✓	✓	84.41
✓	✓			✓	<b>85.71</b>

Table 7: Effect of the Feature Points Redemption compared with (Sun et al. 2021). FPR is our Feature Points Redemption strategy. The U-Net+Seg. refers to (Sun et al. 2021), and Fore. stands for only foreground points transformation.

**the continuous 3D surface texture information.** We substantiate the importance of continuous 3D surface texture information for 3D object detection presented in Table 7. We compare our continuous 2D feature extraction (HD-MK) method with whole scene Feature Point Redemption (FPR) against the binary-segmentation method with the foreground point transformation in (Sun et al. 2021). This method segments foreground points and performs 2D to 3D transformation, disconnecting 3D surface textures between foreground and background. The difference of 1.63% between the second and third rows supports the notion that the absence of continuous 3D surface texture can result in suboptimal performance. Furthermore, the difference of 1.30% between the last two rows indicates our 2D feature extraction method outperforms simple binary segmentation.

**The effectiveness of S-Grid RoI Pooling.** Table 8 shows the effect of our proposed S-Grid RoI Pooling on two different models, i.e., (Shi et al. 2020) and our R<sup>2</sup>Det. We compare each model’s performance with RoI-grid pooling and S-Grid

Method	AP <sub>3D</sub> (%)		
	Easy	Mod.	Hard
PV-RCNN w RoI-grid Pooling	91.31	82.66	80.08
PV-RCNN w RoI-grid Pyramid	92.13	83.13	82.40
PV-RCNN w S-Grid RoI Pooling	92.44	84.77	82.48
<i>Improvement</i>	<i>+0.31</i>	<i>+1.64</i>	<i>+0.08</i>
R <sup>2</sup> Det w RoI-grid Pooling	89.42	83.38	80.20
R <sup>2</sup> Det w RoI-grid Pyramid	91.19	83.82	82.65
R <sup>2</sup> Det w S-Grid RoI Pooling	<b>92.82</b>	<b>85.71</b>	<b>83.36</b>
<i>Improvement</i>	<i>+1.63</i>	<i>+1.89</i>	<i>+0.71</i>

Table 8: Effect of the S-Grid RoI Pooling on the KITTI *val* split with AP calculated by 40 recall positions. RoI-grid Pyramid refers to (Mao et al. 2021a)

RoI pooling, respectively. The results demonstrate that using S-Grid RoI pooling consistently outperforms RoI-grid pooling for both models. This validates that enriching features with various sampling sites is effective in improving the performance of the models. Furthermore, the results suggest that keypoints within a certain radius have a sensitive structure that highly depends on their sampling position, as stated in the Methodology.

## Conclusion

We present R<sup>2</sup>Det, a flexible viewpoint solution for 3D object detection that uses the range view of point clouds as input. Our approach generates range-viewed feature maps using the HD Meta Kernel and uses the Feature Points Redemption module to convert range-view feature points to point view. Proposals are generated from bird’s-eye-view features and refined after S-Grid RoI pooling. Despite using a single-view representation, our approach incorporates information from multiple viewpoints through the Feature Points Redemption module. R<sup>2</sup>Det outperforms all range-view-based approaches and achieves impressive results on both the KITTI dataset and the Waymo Open Dataset. Our findings highlight the importance of addressing 3D surface texture loss in range-view representation and suggest R<sup>2</sup>Det offers an elegant range-view exploration solution for 3D object detection.

## References

- Bewley, A.; Sun, P.; Mensink, T.; Anguelov, D.; and Sminchisescu, C. 2020. Range Conditioned Dilated Convolutions for Scale Invariant 3D Object Detection. In *Conference on Robot Learning*.
- Chen, C.; Chen, Z.; Zhang, J.; and Tao, D. 2022. SASA: Semantics-Augmented Set Abstraction for Point-based 3D Object Detection. In *AAAI Conference on Artificial Intelligence*.
- Chen, T.-H.; and Chang, T. S. 2022. RangeSeg: Range-Aware Real Time Segmentation of 3D LiDAR Point Clouds. *IEEE Transactions on Intelligent Vehicles*, 7: 93–101.
- Chen, X.; Ma, H.; Wan, J.; Li, B.; and Xia, T. 2017. Multi-view 3d object detection network for autonomous driving. In *Proceedings of the IEEE conference on Computer Vision and Pattern Recognition*, 1907–1915.
- Chen, Y.; Liu, J.; Zhang, X.; Qi, X.; and Jia, J. 2023. Voxel-NeXt: Fully Sparse VoxelNet for 3D Object Detection and Tracking. In *Proceedings of the IEEE/CVF Conference on Computer Vision and Pattern Recognition*.
- Cheng, H.-X.; Han, X.-F.; and Xiao, G.-Q. 2023. TransRVNet: LiDAR Semantic Segmentation With Transformer. *IEEE Transactions on Intelligent Transportation Systems*, 24(6): 5895–5907.
- Deng, J.; Shi, S.; Li, P.; Zhou, W.; Zhang, Y.; and Li, H. 2021a. Voxel r-cnn: Towards high performance voxel-based 3d object detection. In *Proceedings of the AAAI Conference on Artificial Intelligence*, 1201–1209.
- Deng, J.; Zhou, W.; Zhang, Y.; and Li, H. 2021b. From multi-view to hollow-3D: Hallucinated hollow-3D R-CNN for 3D object detection. *IEEE Transactions on Circuits and Systems for Video Technology*, 31(12): 4722–4734.
- Fan, L.; Xiong, X.; Wang, F.; Wang, N.; and Zhang, Z. 2021. Rangedet: In defense of range view for lidar-based 3d object detection. In *Proceedings of the IEEE/CVF International Conference on Computer Vision*, 2918–2927.
- Geiger, A.; Lenz, P.; and Urtasun, R. 2012. Are we ready for autonomous driving? The KITTI vision benchmark suite. In *2012 IEEE Conference on Computer Vision and Pattern Recognition*, 3354–3361.
- Graham, B.; and van der Maaten, L. 2017. Submanifold Sparse Convolutional Networks. *ArXiv*, abs/1706.01307.
- He, C.; Li, R.; Li, S.; and Zhang, L. 2022. Voxel Set Transformer: A Set-to-Set Approach to 3D Object Detection from Point Clouds. In *CVPR*.
- He, K.; Zhang, X.; Ren, S.; and Sun, J. 2015. Deep Residual Learning for Image Recognition. *2016 IEEE Conference on Computer Vision and Pattern Recognition (CVPR)*, 770–778.
- Hu, Q.; Yang, B.; Xie, L.; Rosa, S.; Guo, Y.; Wang, Z.; Trigoni, N.; and Markham, A. 2020. Randla-net: Efficient semantic segmentation of large-scale point clouds. In *Proceedings of the IEEE/CVF conference on computer vision and pattern recognition*, 11108–11117.
- Ku, J.; Mozifian, M.; Lee, J.; Harakeh, A.; and Waslander, S. L. 2018. Joint 3d proposal generation and object detection from view aggregation. In *2018 IEEE/RSJ International Conference on Intelligent Robots and Systems (IROS)*, 1–8. IEEE.
- Lang, A. H.; Vora, S.; Caesar, H.; Zhou, L.; Yang, J.; and Beijbom, O. 2019. Pointpillars: Fast encoders for object detection from point clouds. In *Proceedings of the IEEE/CVF conference on computer vision and pattern recognition*, 12697–12705.
- Li, B.; Zhang, T.; and Xia, T. 2016. Vehicle Detection from 3D Lidar Using Fully Convolutional Network. *ArXiv*, abs/1608.07916.
- Li, S.; Geng, K.; Yin, G.; Wang, Z.; and Qian, M. 2023. MVMM: Multi-View Multi-Modal 3D Object Detection for Autonomous Driving. *IEEE Transactions on Industrial Informatics*, 1–9.
- Liang, M.; Yang, B.; Wang, S.; and Urtasun, R. 2018. Deep continuous fusion for multi-sensor 3d object detection. In *Proceedings of the European conference on computer vision (ECCV)*, 641–656.
- Liang, Z.; Zhang, M.; Zhang, Z.; Zhao, X.; and Pu, S. 2020. Rangercnn: Towards fast and accurate 3d object detection with range image representation. *arXiv preprint arXiv:2009.00206*.
- Liang, Z.; Zhang, Z.; Zhang, M.; Zhao, X.; and Pu, S. 2021. RangeIoUDet: Range Image Based Real-Time 3D Object Detector Optimized by Intersection Over Union. In *Proceedings of the IEEE/CVF Conference on Computer Vision and Pattern Recognition (CVPR)*, 7140–7149.
- Liu, Z.; Huang, T.; Li, B.; Chen, X.; Wang, X.; and Bai, X. 2022. EPNet++: Cascade bi-directional fusion for multi-modal 3D object detection. *IEEE Transactions on Pattern Analysis and Machine Intelligence*.
- Mahmoud, A.; Hu, J. S.; and Waslander, S. L. 2023. Dense voxel fusion for 3D object detection. In *Proceedings of the IEEE/CVF Winter Conference on Applications of Computer Vision*, 663–672.
- Mao, J.; Niu, M.; Bai, H.; Liang, X.; Xu, H.; and Xu, C. 2021a. Pyramid r-cnn: Towards better performance and adaptability for 3d object detection. In *Proceedings of the IEEE/CVF International Conference on Computer Vision*, 2723–2732.
- Mao, J.; Xue, Y.; Niu, M.; Bai, H.; Feng, J.; Liang, X.; Xu, H.; and Xu, C. 2021b. Voxel Transformer for 3D Object Detection. In *ICCV*.
- Meyer, G. P.; Laddha, A.; Kee, E.; Vallespi-Gonzalez, C.; and Wellington, C. K. 2019. Lasernet: An efficient probabilistic 3d object detector for autonomous driving. In *Proceedings of the IEEE/CVF conference on computer vision and pattern recognition*, 12677–12686.
- Milioto, A.; Vizzo, I.; Behley, J.; and Stachniss, C. 2019. Rangenet++: Fast and accurate lidar semantic segmentation. In *2019 IEEE/RSJ international conference on intelligent robots and systems (IROS)*, 4213–4220. IEEE.
- Nowak, T.; Ćwian, K.; and Skrzypczyński, P. 2021. Real-Time Detection of Non-Stationary Objects Using Intensity Data in Automotive LiDAR SLAM. *Sensors*, 21(20).



- Qi, C.; Liu, W.; Wu, C.; Su, H.; and Guibas, L. J. 2017a. Frustum PointNets for 3D Object Detection from RGB-D Data. *2018 IEEE/CVF Conference on Computer Vision and Pattern Recognition*, 918–927.
- Qi, C. R.; Su, H.; Mo, K.; and Guibas, L. J. 2017b. Pointnet: Deep learning on point sets for 3d classification and segmentation. In *Proceedings of the IEEE conference on computer vision and pattern recognition*, 652–660.
- Qi, C. R.; Yi, L.; Su, H.; and Guibas, L. J. 2017c. Pointnet++: Deep hierarchical feature learning on point sets in a metric space. *Advances in neural information processing systems*, 30.
- Shi, S.; Guo, C.; Jiang, L.; Wang, Z.; Shi, J.; Wang, X.; and Li, H. 2020. Pv-rcnn: Point-voxel feature set abstraction for 3d object detection. In *Proceedings of the IEEE/CVF Conference on Computer Vision and Pattern Recognition*, 10529–10538.
- Shi, S.; Wang, X.; and Li, H. 2019. Pointnet++: 3d object proposal generation and detection from point cloud. In *Proceedings of the IEEE/CVF conference on computer vision and pattern recognition*, 770–779.
- Sun, P.; Kretschmar, H.; Dotiwalla, X.; Chouard, A.; Patnaik, V.; Tsui, P.; Guo, J.; Zhou, Y.; Cai, Y.; Caine, B.; et al. 2020. Scalability in perception for autonomous driving: Waymo open dataset. In *Proceedings of the IEEE/CVF conference on computer vision and pattern recognition*, 2446–2454.
- Sun, P.; Wang, W.; Chai, Y.; Elsayed, G.; Bewley, A.; Zhang, X.; Sminchisescu, C.; and Anguelov, D. 2021. Rsn: Range sparse net for efficient, accurate lidar 3d object detection. In *Proceedings of the IEEE/CVF Conference on Computer Vision and Pattern Recognition*, 5725–5734.
- Wang, Y.; Fathi, A.; Kundu, A.; Ross, D. A.; Pantofaru, C.; Funkhouser, T.; and Solomon, J. 2020. Pillar-based object detection for autonomous driving. In *European Conference on Computer Vision*, 18–34. Springer.
- Wang, Z.; and Jia, K. 2019. Frustum ConvNet: Sliding Frustums to Aggregate Local Point-Wise Features for Amodal. *2019 IEEE/RSJ International Conference on Intelligent Robots and Systems (IROS)*, 1742–1749.
- Wu, B.; Wan, A.; Yue, X.; and Keutzer, K. 2018. SqueezeSeg: Convolutional neural nets with recurrent crf for real-time road-object segmentation from 3d lidar point cloud. In *2018 IEEE international conference on robotics and automation (ICRA)*, 1887–1893. IEEE.
- Xiao, W.; Peng, Y.; Liu, C.; Gao, J.; Wu, Y.; and Li, X. 2023. Balanced Sample Assignment and Objective for Single-Model Multi-Class 3D Object Detection. *IEEE Transactions on Circuits and Systems for Video Technology*, 1–1.
- Yan, Y.; Mao, Y.; and Li, B. 2018. SECOND: Sparsely Embedded Convolutional Detection. *Sensors*, 18(10): 3337.
- Yang, B.; Liang, M.; and Urtasun, R. 2018. Hdnet: Exploiting hd maps for 3d object detection. In *Conference on Robot Learning*, 146–155. PMLR.
- Yang, H.; He, T.; Liu, J.; Chen, H.; Wu, B.; Lin, B.; He, X.; and Ouyang, W. 2023a. GD-MAE: generative decoder for MAE pre-training on lidar point clouds. In *Proceedings of the IEEE/CVF Conference on Computer Vision and Pattern Recognition*, 9403–9414.
- Yang, H.; Wang, W.; Chen, M.; Lin, B.; He, T.; Chen, H.; He, X.; and Ouyang, W. 2023b. PVT-SSD: Single-Stage 3D Object Detector with Point-Voxel Transformer. In *Proceedings of the IEEE/CVF Conference on Computer Vision and Pattern Recognition*, 13476–13487.
- Yang, Z.; Sun, Y.; Liu, S.; and Jia, J. 2020. 3dssd: Point-based 3d single stage object detector. In *Proceedings of the IEEE/CVF conference on computer vision and pattern recognition*, 11040–11048.
- Yang, Z.; Sun, Y.; Liu, S.; Shen, X.; and Jia, J. 2018. IPOD: Intensive Point-based Object Detector for Point Cloud. *ArXiv*, abs/1812.05276.
- Zhang, Y.; Chen, J.; and Huang, D. 2022. CAT-Det: Contrastively Augmented Transformer for Multi-Modal 3D Object Detection. In *Proceedings of the IEEE/CVF Conference on Computer Vision and Pattern Recognition (CVPR)*, 908–917.
- Zhang, Y.; Hu, Q.; Xu, G.; Ma, Y.; Wan, J.-H.; and Guo, Y. 2022. Not All Points Are Equal: Learning Highly Efficient Point-based Detectors for 3D LiDAR Point Clouds. *2022 IEEE/CVF Conference on Computer Vision and Pattern Recognition (CVPR)*, 18931–18940.
- Zheng, W.; Tang, W.; Chen, S.; Jiang, L.; and Fu, C.-W. 2020. CIA-SSD: Confident IoU-Aware Single-Stage Object Detector From Point Cloud. In *AAAI Conference on Artificial Intelligence*.
- Zheng, Z.; Huang, Z.; Zhao, J.; Hu, H.; and Chen, D. 2023. DTSSD: Dual-Channel Transformer-Based Network for Point-Based 3D Object Detection. *IEEE Signal Processing Letters*, 30: 798–802.
- Zhou, C.; Zhang, Y.; Chen, J.; and Huang, D. 2023. OcTr: Octree-based Transformer for 3D Object Detection. In *CVPR*.
- Zhou, Y.; Sun, P.; Zhang, Y.; Anguelov, D.; Gao, J.; Ouyang, T.; Guo, J.; Ngiam, J.; and Vasudevan, V. 2020. End-to-end multi-view fusion for 3d object detection in lidar point clouds. In *Conference on Robot Learning*, 923–932. PMLR.
- Zhou, Y.; and Tuzel, O. 2017. VoxelNet: End-to-End Learning for Point Cloud Based 3D Object Detection. *2018 IEEE/CVF Conference on Computer Vision and Pattern Recognition*, 4490–4499.